Article

A Systematic Investigation of *p*-Nitrophenol Reduction by Bimetallic Dendrimer Encapsulated Nanoparticles

Zachary D. Pozun,[†] Stacia E. Rodenbusch, Emily Keller, Kelly Tran, Wenjie Tang, Keith J. Stevenson,* and Graeme Henkelman*

Department of Chemistry and Biochemistry, University of Texas at Austin, Austin, Texas 78712, United States

ABSTRACT: We demonstrate that the reduction of *p*-nitrophenol to *p*-aminophenol by $NaBH_4$ is catalyzed by both monometallic and bimetallic nanoparticles (NPs). We also demonstrate a straightforward and precise method for the synthesis of bimetallic nanoparticles using poly(amido)amine dendrimers. The resulting dendrimer encapsulated nanoparticles (DENs) are monodisperse, and the size distribution does not vary with different elemental combinations. Random alloys of Pt/Cu, Pd/Cu, Pd/Au, Pt/Au, and Au/Cu DENs were synthesized and evaluated as catalysts for *p*-nitrophenol reduction. These combinations are chosen in order to selectively tune the binding energy of the *p*-nitrophenol adsorbate to the nanoparticle surface. Following the Brønsted−Evans−Polanyi (BEP) relation, we show that the binding energy can reasonably predict the reaction rates of *p*-nitrophenol reduction. We demonstrate that the measured reaction rate constants of the bimetallic DENs is not always a simple average of the properties of the constituent metals. In particular, DENs containing metals with similar lattice constants produce a binding energy close to the average of the two constituents, whereas DENs containing metals with a lattice mismatch show a bimodal distribution of binding energies. Overall, in this work we present a uniform method for synthesizing pure and bimetallic DENs and demonstrate that their catalytic properties are dependent on the adsorbate's binding energy.
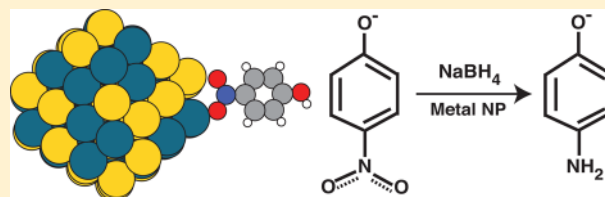
INTRODUCTION

Catalysis at the nanoscale has attracted significant attention in the past two decades due to the unique properties of materials that arise at the nanoscale.[1] Following the discovery by Valden et al.[2] of catalytically active gold nanoclusters, gold, in particular, has become the basis for novel catalysts due to its activity at the nanoscale. Metal nanocatalysts have found a wide range of applications including CO oxidation,[3] carbon nanotube nucleation,[4] alcohol dehydrogenation,[5] and formic acid electrooxidation.[6] In particular, nanocatalysts have played an extensive role in fuel cell catalysts by reducing oxygen[7,8] and oxidizing methanol.[9] Theoretical tools have allowed for the prediction of novel catalysts for oxygen reduction,[10] olefin/paraffin separations,[11,12] and ammonia synthesis.[13]

Bimetallic nanoparticles are particularly useful due to the additional degrees of freedom—composition and structure—that may be adjusted in order to improve catalytic behavior. Bimetallic catalysts frequently display catalytic activity that is higher than either constituent material. For instance, two epitaxially grown overlayers of Pd on Au have been predicted to bind CO stronger than either pure metal.[14] Similar effects have been exploited in the Ni/Au bimetallic system in order to design a steam reforming catalyst with a higher efficiency.[15]

The interplay between geometry and electronic structure has been extensively studied both theoretically and experimentally for bimetallic systems in order to determine how these factors affect the catalytic properties of these materials.[16] The role of electronic structure in metals, specifically the *d*-band center, was first modeled by Newns[17] and later expanded upon with first principles calculations by Hammer and Nørskov.[18] This model, which relates the *d*-band center with binding energy, has been applied to CO adsorption on bimetallic systems,[19] hydrogenation of olefins by bimetallics,[20] nitrobenzene hydrogenation by bimetallic nanoclusters,[21] and many other surface reactions.

First-order surface reactions, which are of particular importance for catalysis, are typically constrained to a linear relationship between adsorption energy and reaction rate. This correlation, the Brønsted−Evans−Polanyi (BEP) relation,[22,23] has been demonstrated to fundamentally constrain many surface reactions.[24] The BEP relation predicts that strong adsorption energies to the surface result in faster reaction rates for first-order surface reactions.

In practice, the turnover frequency of a catalyst is limited in both the weak binding and strong binding regimes. In the strong binding regime where the BEP relation shows the smallest reaction barriers, the catalytic performance is limited by the desorption of products. In the weak binding regime, the reaction rate is limited by the large activation energies predicted by BEP. An optimal catalyst will balance these two regimes such that the barriers are low enough to be overcome and that the adsorbed molecules may diffuse and desorb from the surface.

The balance between these two regimes is described graphically by the so-called volcano plot.[25] The volcano plot,

a scatter plot of turnover frequency as a function of adsorption energy, peaks at the center and avoids both the weak and strong binding limits. By using bimetallic DENs, we demonstrate that a catalyst for *p*-nitrophenol (PNP) reduction may be designed by tuning DEN composition and structure in order to bind the product molecule with an adsorption energy closest to the peak in the volcano plot.

PNP, as with other nitrophenols and derivatives, is a common byproduct from the production of pesticides, herbicides, and synthetic dyes.[26] PNP is easily reduced by $NaBH_4$ in the presence of metals in solution.[27,28] Coinage metals, in particular, have been demonstrated to be excellent catalysts for PNP reduction at the nanoscale.[29] Bimetallic coinage metal nanoparticles have been demonstrated to catalyze PNP reduction with rates that strongly differ from a simple linear interpolation between the rates of the two pure metals.[30] These types of bimetallic nanoparticles may be easily synthesized in solution with dendrimer encapsulation methods that allow for precise control over particle size and composition.[31,32]

Experimentally, PNP has a strong absorption at 400 nm,[33] which allows for an easy and reliable means to measure reaction rates by UV−vis spectroscopy. The overall reaction rate is pseudo-first-order when both the metal catalyst and $NaBH_4$ are in excess.[34] The reduction of PNP is, thus, an ideal model system for demonstrating the BEP relation for pseudo-first-order reactions and the tunability of bimetallic nanoparticles in order to produce an optimal catalyst. Reduction of PNP on Au nanoparticles has been demonstrated to follow Langmuir−Hinshelwood mechanism statistics.[35] In this mechanism, both molecules adsorb onto a surface before undergoing the bimolecular reaction. When $NaBH_4$ is in excess, the rate is controlled by the adsorption of PNP.

We apply a joint computational−experimental approach in order to tune the reaction rate of PNP reduction by adjusting the composition of the metal nanoparticle catalysts. In particular, we show that the BEP relation accurately represents this type of multistep, pseudo-first-order reaction and that bimetallic DENs can be used to approach the peak in the resulting volcano plot. This systematic study demonstrates that theoretically predicted adsorption energies onto simple bimetallic surfaces provide a simple and accurate predictor for catalytic reaction rates in pseudo-first-order reactions. We note that when the lattice constants of the constituent metals of the bimetallic nanoparticles are similar, the resulting properties are essentially a linear combination of the properties of the two pure metals. In contrast, large lattice constant mismatches result in a bimodal distribution of catalytic properties.

■ METHODS

Experimental Details. The synthesis of AuCu, PdCu, and PtCu DENs was reviewed by Yeung and Crooks.[36] Hoover et al.[37] also described the synthesis of PtCu. The synthesis of PtPd was described by Ye and Crooks.[38] Scott et al.[39] described the synthesis of PdAu. Preparation of PtAu bimetallic particles by cocomplexation in G6-OH dendrimers has not been previously reported, but the UV−vis spectra presented here match those for bimetallic PtAu DENs prepared by Lang et al.[3] using galvanic exchange.

Materials. $NaBH_4$ was purchased from EMD, $HAuCl_4$ was purchased from Acros Organics, $CuSO_4$ was purchased from Mallinckrodt, and both K_2PdCl_4 and K_2PtCl_4 were purchased from Alfa Aesar. All chemicals were used as received, without

further purification. All solutions were prepared with water acquired from a Barnstead NANOpure Diamond UV Deionization System, >18.2 MOhm·cm (denoted as "nanopure water"). G6-OH PAMAM dendrimer (13.22% w/w in methanol) was a donation from Dendritech, Inc.

G6-OH(M55-56) DEN Synthesis. Each dendrimer solution was prepared by evaporating the methanol from 5.46 μL of G6-OH PAMAM dendrimer in a 20 mL vial (I-Chem) with septum cap. The dendrimer was hydrated with enough nanopure water to result in a final volume of 10 mL and a final dendrimer concentration of 1 μM after the addition of metal salt, the pH adjustment, and the addition of reductant. For a 55 molar excess of metal-to-dendrimer, 5.5 μL of 0.1 M metal salt was added. The pH of the solution was adjusted to 6−7 using 0.1 M HCl. The vial was capped and left on a nutating mixer to complex.

Complexation time was dependent on the metal salt used: $HAuCl_4$ was complexed for <10 min, $CuSO_4$ for 15 min, K_2PdCl_4 for 30−60 min, and K_2PtCl_4 for 72 h. Dendrimer−metal complexes were reduced with a 10 molar excess of $NaBH_4$ to metal (except Au, for which only 1−2 molar excess was used) by adding freshly prepared 0.2 M $NaBH_4$. The pH of the reduced nanoparticle solution was adjusted to <8 using 0.1 M HCl. The solution was purged with Ar(g) for 10 min. The DENs were characterized via UV−vis spectroscopy prior to and immediately after reduction.

Bimetallic DENs were synthesized as described above, except only a 28 molar excess of each metal was added (2.8 μL of 0.1 M metal salt). The longer complexing metal salt was added first, the pH was adjusted to 6−7, and then at the appropriate time before reduction, the second metal salt was added.

UV−vis Spectroscopy. UV−vis spectra were collected using a spectral bandwidth of 1.0 nm with an Agilent 8453 UV−vis diode array spectrophotometer and Agilent ChemStation software. Samples were measured in a quartz cuvette with a 1 cm path length.

Kinetic Measurements. Fresh 0.2 M $NaBH_4$ was prepared 10 min before each set of kinetic trials. Polystyrene cuvettes were prepared by adding 2.35 mL of nanopure and 0.250 mL of 600 μM PNP. An Ocean Optics Visible Spectrophotometer was set to monitor the absorbance at 400 nm (the λ_{max} for PNP) and 600 nm (for background) by sampling three times per second. The spectrophotometer was placed on a stir plate, and a microstir bar was added to the reaction cuvette. Immediately after initiating data collection, 0.750 mL of 0.2 M $NaBH_4$ was added to the cuvette using a micropipet (Gilson) and 0.600 mL of 1 μM DEN solution was added to the cuvette via gastight syringe.

Calculation of Kinetic Rate Constants. The data were analyzed according to the first-order rate law. The absorbance at 400 nm was used to determine the concentration of PNP. The minimum absorbance at 400 nm was subtracted from all absorbances to correct for background absorption from the DENs. The natural log of the absorbance at 400 nm was plotted against time, and the steepest part of the curve was fit with a line, the negative slope of which was considered the apparent rate constant, k_{app}. The rate constant is considered apparent because previous work by other groups has shown that the observed rate constant depends on the concentration of sodium borohydride as well as the starting concentration of PNP.[35]

Computational Details. All calculations were performed by density functional theory (DFT) within the Vienna *ab initio* Simulation Package.[40−43] The Kohn−Sham[44] single-electron

orbitals for the valence were expanded in a plane-wave basis with an energy cutoff of 300 eV. Core electrons were described as pseudopotentials within the projector-augmented wave formalism.[45,46] The exchange-correlation (XC) energy was treated by the PW91 implementation of the generalized-gradient approximation.[47−49] The interpolation of the XC term was performed using the method of Vosko et al.[50]

The Brillouin zone was integrated using the Methfessel−Paxton finite temperature smearing approach with a smearing width σ of 0.2 eV.[51] A Γ-point sampling was employed. All energies were extrapolated to the $\sigma \rightarrow 0$ limit. Adsorption was considered on the (100) face of a 79-atom nanoparticle in a truncated octahedron geometry, which was found to be the most stable for Pt by both total X-ray scattering experiment and DFT calculations.[52] This face is the most undercoordinated and taken to be the most active for catalysis. The PNP molecule was then allowed to adsorb onto the surface such that the total force per atom was less than 0.01 eV/Å. This bonding geometry is shown for a sample Pd/Au random alloy in Figure 1. For each bimetallic system, ten random 50/50 alloys by composition were generated; geometries that significantly distorted from the truncated octahedron were removed.
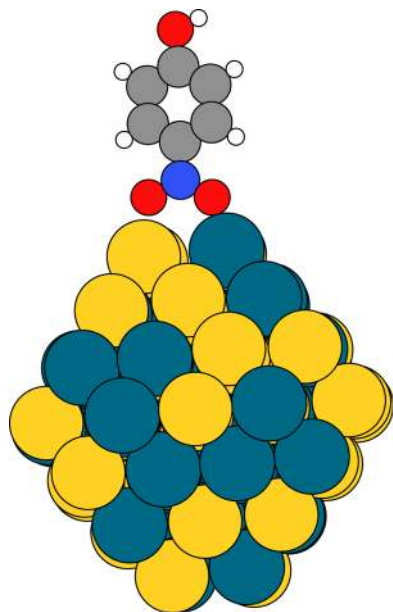
Figure 1. Chosen binding geometry for PNP chemisorption on a 79-atom Pd/Au random alloy nanoparticle.

At least 8 Å of vacuum was included to separate periodic images in order to prevent spurious image−image interaction. For density of states (DOS) calculations, the bulk lattice constants calculated by Wang et al.[53] were used for a cell that consisted of five layers of the 3×3 face-centered cubic unit cell. The Brillouin zone for the unit cell was integrated using a $4 \times 4 \times 1$ Monkhorst−Pack k-point mesh.[54]

Adsorption energies were determined by calculating the difference between the total energy of the relaxed nanoparticle−PNP chemisorbed complex and the total energies of the two constituent pieces: the nanoparticle and the PNP molecule. Thus, the adsorption energy represents the energy difference between taking the PNP molecule from infinite distance and allowing it to chemisorb onto the nanoparticle surface. The binding energy, which has the opposite sign from

the adsorption energy, represents the energy required to separate the bound PNP molecule from the nanoparticle and move it to infinite distance.

■ RESULTS AND DISCUSSION

In order to accurately compare reaction rates for different catalysts, a systematic and uniform method for both synthesizing the catalyst and maintaining similar reaction conditions is required. Through an encapsulation synthesis route using the G6-OH PAMAM dendrimer, we are able to reliably synthesize nanoparticles of similar size and with known composition. This synthetic route produces nanoparticles of either pure metals or bimetallic random alloys with a 50/50 composition. Figure 2 shows scanning transmission electron microscopy (STEM) images and size distribution histograms for the synthesis of Au, Pd, and Pd/Au nanoparticles.
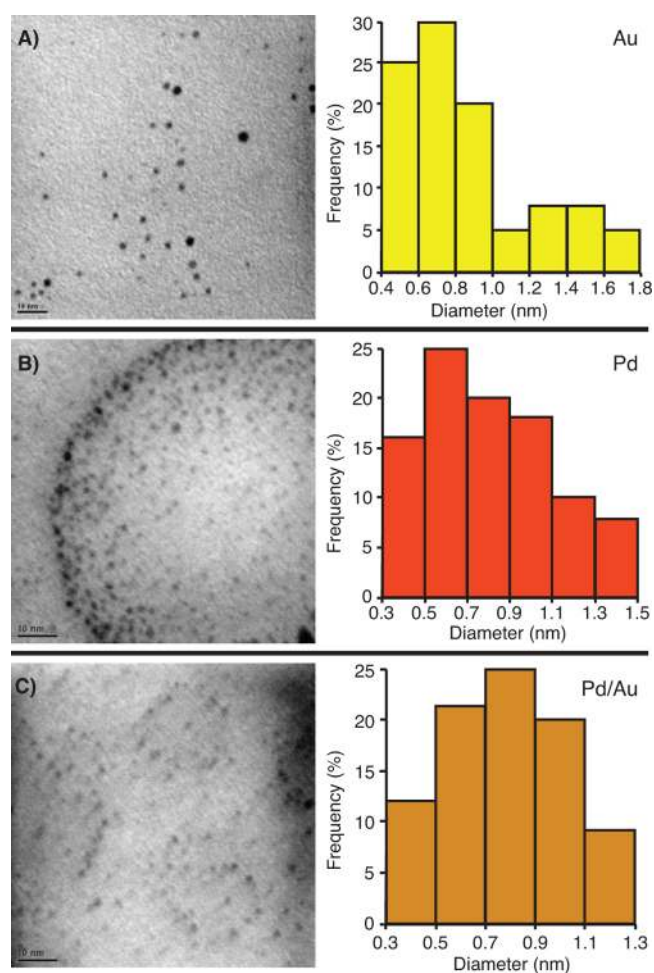

Figure 2. STEM images of DENs (A) G6-OH(Au$_{55}$), (B) G6-OH(Pd$_{55}$), and (C) G6-OH(Pd$_{28}$Au$_{28}$) and corresponding size distributions. The average diameter of the Au, Pd, and Pd/Au nanoparticles was 1.4 ± 0.7, 1.0 ± 0.3, and 1.1 ± 0.3 nm, respectively. Images were collected on a JEOL 2500SE STEM.

As seen in Figure 2, DENs of Au, Pd, and Pd/Au have very similar average diameters on the order of 1 nm. The DENs are spherical in shape; given the size distributions and shape, the nanoparticles contain ∼55 atoms. As noted previously, the experimental conditions are nearly uniform for each pure metal and bimetallic nanoparticle synthesis route. Because of these

tight experimental controls, we can directly measure catalytic properties of the resulting particles under both uniform synthesis and reaction conditions.

The reduction of PNP in the presence of NaBH₄ is fast when performed in solution with coinage metal catalysts. The overall reaction of interest is shown in Scheme 1. The full catalytic

Scheme 1. Reaction Scheme for the Reduction of _p_-Nitrophenol to _p_-Aminophenol[a]
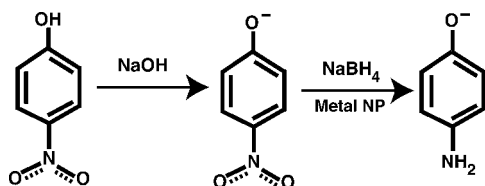
[a]Because _p_-nitrophenol is insoluble in water, it is first dissolved in NaOH. The resulting nitrophenolate is then reduced via sodium borohydride in the presence of the metal catalyst.

reaction, however, is a multistep process that is not characterized by a single saddle point from which an Arrhenius rate may be extracted. In the presence of excess NaBH₄ and sufficient catalyst, the reaction is pseudo-first-order and dependent only upon the concentration of PNP in solution. The role of the metallic catalyst is to bind the PNP molecule through the two oxygens of the nitro group. This adsorbed geometry is shown in Figure 1, where a single molecule binds to two atoms of a (100) surface and creates a pentagonal M−O−N−O−M cyclic intermediate.

PNP is a strong visible absorber with a maximum absorbance at 400 nm. As shown in Figure 3, the reduction of PNP to _p_-aminophenol (PAP) is evidenced by a decrease in absorbance at 400 nm and a new absorbance growing in at 315 nm associated with formation of PAP. Because the reaction is pseudo-first-order in the presence of excess NaBH₄, the slope of a plot of the natural log of the absorbance at 400 nm yields the apparent reaction rate, k_{app}. This process for determining apparent rates is shown in Figure 3 for the case of the Pd/Cu alloy. Thus, we show that the reaction rates can be easily determined by ultraviolet−visible (UV−vis) spectroscopy.

Because of the sole dependence of the rate on the concentration of PNP in solution, the initial adsorption of the PNP molecule to the nanoparticle surface directly correlates with the rate constant for the full reaction. Binding of organic molecules to metal surfaces has been extensively modeled beginning with Newns[17] and later expanded upon by Hammer and Nørskov.[18,19,55−57]

The Hammer−Nørskov model identifies the center of the _d_-band of the metal surface as the primary controlling factor in chemisorption strength. When the adsorbate interacts with the metal _d_-band, the adsorbate state overlaps with the metal states and is split off into bonding and antibonding interactions. As the _d_-band becomes farther below the Fermi energy, the antibonding states are increasingly populated, and the overall chemisorption strength weakens. A scatter plot of the _d_-band against the adsorption energy is shown in Figure 4.

From Figure 4, a general trend of increasing adsorption strength with a _d_-band center closer to the Fermi energy is noted. A further trend, however, is that adsorption energy decreases as one moves down columns of the periodic table. This effect has been noted by Hammer[57] for oxygen adsorption onto noble metals. For the coinage metals, the _d_-band is nearly
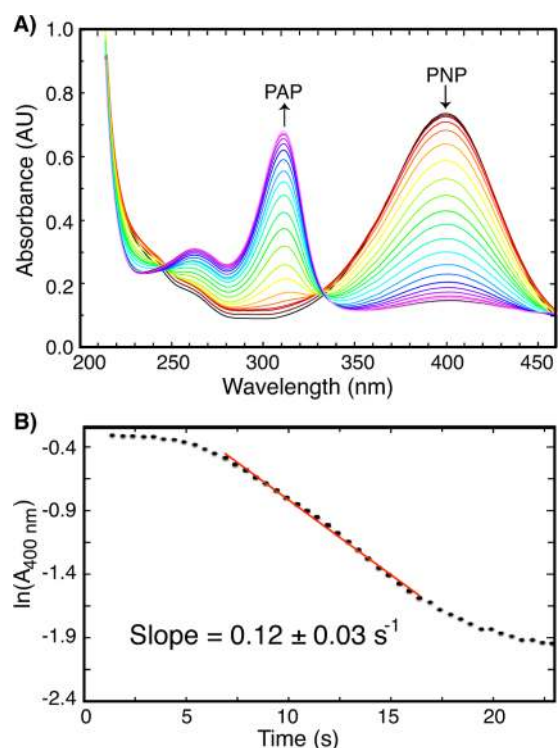
Figure 3. Reduction of PNP catalyzed by DENs, monitored by UV−vis. (A) shows the decreasing absorbance at 400 nm corresponding to decreasing PNP concentration; spectra are shown at 1 s intervals. (B) shows the plot of the natural log of the absorbance at 400 nm versus time; data points are separated by 0.5 s intervals. The slope in (B) yields the apparent rate constant $k_{app} = 0.12 \pm 0.03$ (s⁻¹) for this trial. G6-OH(Pd₂₈Cu₂₈) DENs were used for this trial.
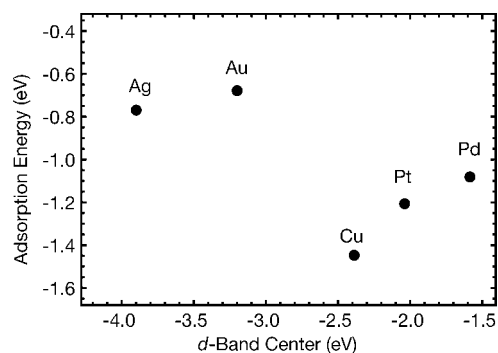
Figure 4. A scatter plot of the _d_-band center of the metal surface vs the adsorption strength of _p_-nitrophenol shows a general increasing binding interaction with a _d_-band center closer to the Fermi energy. The _d_-band center is a weighted average of the local DOS for a single surface atom.

filled, so many antibonding states are populated. The population of bonding and antibonding states is net repulsive, which increases with orbital size as one moves down a column. This increasingly repulsive interaction for the coinage metals accounts for the weaker adsorption onto Pt and Pd rather than Cu, despite the differences in _d_-band centers.

When disparate metals are alloyed, charge rearranges due to the disparate Fermi levels that are brought into contact. Because of charge rearrangement, noble metal atoms become less noble and reactive metal atoms become less reactive.[10,58] In addition, alloying of metals from different rows on the periodic

table has been demonstrated to activate surfaces by introducing localized electronic states.[12] For instance, small amounts of Au alloyed into previously inert Ag(111) surfaces allow it to bind ethylene. The $5d$ electrons of the Au atoms overlap poorly with the $4d$ of the Ag surface and create localized states where ethylene may bind.

Because of the direct dependence of the reaction rate constant on the binding energy, our goal is to optimize the reactivity of bimetallic DENs by combining metals which are inactive due to strongly binding the reactants with metals that are inactive due to weakly binding the reactants. This relationship is typically demonstrated via a volcano plot, which is a scatter plot of the reaction rate in the presence of the catalyst against the adsorption energy of the reactant to the catalyst. In principle, overly strong binding renders the adsorbate−catalyst so strongly bound that a reaction cannot occur. In the regime of overly weak binding, the catalyst has no interaction with the reactant. The peak in the volcano occurs where these two effects are balanced.

We consider chemisorption onto the (100) face of the truncated octahedron NP as a representative site for chemisorption onto the synthesized NPs in solution. Chemisorption onto the (100) face is possible in both truncated octahedron and cuboctahedron geometries; effects from undercoordination are likely to be smaller than 0.1 eV.[12] In Figure 5, we present a volcano plot of calculated adsorption
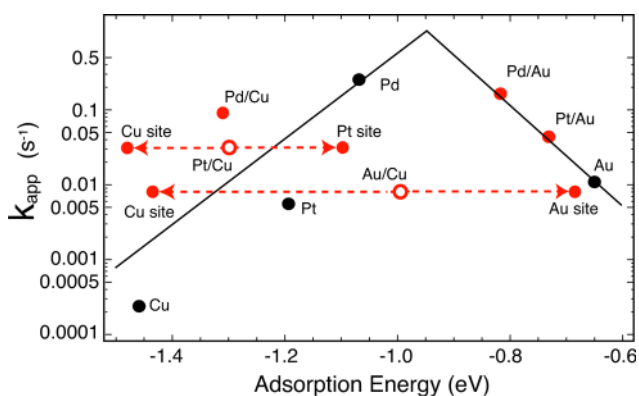

Figure 5. A scatter plot of the calculated adsorption energy of PNP on various nanoparticles plotted against the experimentally observed reaction rates. Solid black dots are pure metals, and red dots are random alloys of two metals. The solid lines are best-fit lines for the strong- and weak-binding regimes. The dashed lines represent the range of calculated binding energies for various allowed structures that were considered.

energies of the PNP molecule onto the various nanoparticle catalysts plotted with the experimentally measured reaction rates for PNP reduction. In this plot, two regimes of overbinding and underbinding are identifiable. Of the pure metals, Au has a low reaction rate constant due to its weak binding, whereas Cu has a very low rate constant due to its overly strong binding. Pt and Pd fall between these extremes.

One effect that is immediately noticeable in Figure 5 is that alloying Au with either Pt or Pd results in a stronger binding energy and yields a correspondingly faster reaction rate constant. When Pd is alloyed with Cu, the adsorption energy is much stronger than as compared to pure Pd and is followed by a slower reaction rate. Somewhat surprisingly, then, is the behavior of Pt/Cu, which has a higher reaction rate than either

pure Pt or pure Cu. Even worse, Au/Cu would seem to have an average adsorption energy that sits very near to the peak in the volcano, and yet it has a reaction rate that is very close to pure Au.

The solution to this seeming paradox lies in the distribution of the adsorption energies for different configurations of the bimetallic alloys. Cu is much smaller than either Pt or Au, so the lattice constant mismatch compresses the atoms in the system. Similarly, the $3d$ Cu valence orbitals overlap very weakly with the $5d$ orbitals of Pt and Au. The net result is that configurations in which PNP is bound to two Cu atoms is bound quite strongly and is bound weakly when Au or Pt is present. The range in the binding energy data is shown in Figure 6, which shows that Pd/Cu displays a unimodal
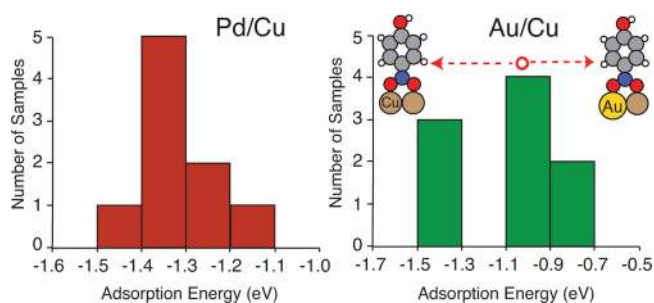
Figure 6. Histograms of the adsorption energies of PNP on nanoparticles of Pd/Cu and Au/Cu are shown. The y-axis of the histogram is the number of nanoparticles in the randomly generated sample of bimetallic alloys of the specified composition, and the x-axis is the binding energy of PNP. The Pd/Cu distribution is centered around a single ensemble average for binding energy; however, the Au/Cu binding energy has two peaks that correspond to the pure Cu site and the Au−Cu site.

distribution centered around the average of Pd and Cu, whereas Au/Cu displays binding energies that correspond to either binding strongly on two Cu atoms or weakly when Au is present.

In addition, the fact that alloying with Cu weakens the adsorption energy on Pt and Au atoms compared with the pure is also explained by the d-band model. When a metal with a large lattice constant is compressed by alloying with a smaller metal, the orbital overlap between its atoms increases. The effect of this compression is that the d-band center shifts away from the Fermi level; this effect results in decreased reactivity at the site of compression.[12] Because of this decrease in d-band center, the larger metal atoms become less likely to form a covalent bond with an adsorbate. This effect is demonstrated by the fact that two Pt atoms bind PNP weaker in the alloy than in the pure nanoparticle. More pronounced, two Au atoms bind PNP in a pure nanoparticle significantly stronger than in the alloy, where the two Au atoms are forced closer together.

Thus, the effect on the reaction rate is significant. A change in adsorption energy results in an exponential change in the reaction rate. Thus, the system reacts at the rate of its most active component along the volcano plot. The molecule is too strongly adsorbed on Cu, so the reaction rate is controlled by the orders of magnitude faster rate associated with binding at an Au−Cu two-atom site. In the case of Pt/Cu, two Pt atoms bind PNP weaker than two Pt atoms in a pure metal nanoparticle; thus, the reaction rate is faster than pure Pt. The ensemble binding energies, represented by the two data points, are less significant to predicting the overall reaction rate

than the spread in the data and the maxima and minima of adsorption energies in the set of random alloys.

These results suggest a largely unexpected strategy in generating bimetallic catalysts. In particular, we show that for metals of similar lattice constants, one can alloy a metal that binds the target molecule too strongly with one that binds it too weakly to yield a more active particle. In contrast, when the lattice constants are disparate, the results do not follow this trend. Instead, the resulting adsorption energies are broadly distributed, so the overall ensemble average of binding energy can be completely uncorrelated from the observed reaction rate. In this case, catalysts with a specific geometry at the binding site are the most active and dominate the reaction rate. The result is that two metals that bind too strongly can alloy to create a significantly more active catalyst, even though the average binding energy appears to be unfavorable.

CONCLUSIONS

In summary, we have presented a systematic method for the synthesis of uniform pure and bimetallic nanoparticles using a dendrimer-encapsulation synthesis route. This systematic synthesis method leads naturally into controlled, uniform reaction conditions for measuring catalytic activity of PNP reduction in presence of sodium borohydride. In this manner, reaction rates for similar particles under the same reaction conditions can be accurately measured and compared to binding energies from electronic structure calculations. We demonstrate that the reaction rates fall along a standard volcano plot.

In order to selectively tune the reaction rate toward the maximum in the volcano plot, we produced several bimetallic catalysts. For alloys of metals with similar lattice constants, the result was perfectly intuitive—the ensemble binding energy was the average of the two metals. In this case, the reaction rates fell along the volcano plot as expected. In contrast, metals with dissimilar lattice constants—Pt/Cu and Au/Cu—did not fall along the volcano plot as predicted. Pt/Cu catalyzed the reaction much faster than expected from the ensemble binding energy, and Au/Cu catalyzed it much slower than expected. We demonstrated that the reaction rate was not controlled by the ensemble binding energy, but by the binding energy of the most active metal atoms, whose binding energies were quite different from the ensemble average. Overall, we have demonstrated a joint experimental—theoretical method for evaluating catalysis by bimetallic and pure DENs and analyzed the factors, such as lattice mismatch, that determine whether or not the properties of a bimetallic will be a simple average of the constituents' properties.

AUTHOR INFORMATION

Corresponding Author
*E-mail: stevenson@cm.utexas.edu (K.J.S.); henkelman@cm.utexas.edu (G.H.).

Present Address
†Z.D.P.: Department of Chemistry, University of Pittsburgh, Pittsburgh, PA 15260.

Notes
The authors declare no competing financial interest.

ACKNOWLEDGMENTS

REFERENCES

(1) Toshima, N.; Yonezawa, T. Bimetallic Nanoparticles-Novel Materials for Chemical and Physical Applications. *New J. Chem.* **1998**, *22*, 1179−1201.

(2) Valden, M.; Lai, X.; Goodman, D. W. Gold Clusters on Titania with the Appearance of Nonmetallic Properties. *Science* **1998**, *281*, 1647−1650.

(3) Lang, H.; Maldonado, S.; Stevenson, K. J.; Chandler, B. D. Synthesis and Characterization of Dendrimer Templated Supported Bimetallic Pt-Au Nanoparticles. *J. Am. Chem. Soc.* **2004**, *126*, 12949−12956.

(4) Ago, H.; Murata, K.; Yumura, M.; Yotani, J.; Uemura, S. Ink-Jet Printing of Nanoparticle Catalyst for Site-Selective Carbon Nanotube Growth. *Appl. Phys. Lett.* **2003**, *82*.

(5) Mitsudome, T.; Mikami, Y.; Funai, H.; Mizugaki, T.; Jitsukawa, K.; Kaneda, K. Oxidant-Free Alcohol Dehydrogenation Using a Reusable Hydrotalcite-Supported Silver Nanoparticle Catalyst. *Angew. Chem.* **2008**, *120*, 144−147.

(6) Waszczuk, P.; Barnard, T. M.; Rice, C.; Masel, R. I.; Wieckowski, A. A Nanoparticle Catalyst with Superior Activity for Electrooxidation of Formic Acid. *Electrochem. Commun.* **2002**, *4*, 599−603.

(7) Vijayaraghavan, G.; Stevenson, K. J. Synergistic Assembly of Dendrimer Templated Platinum Catalysts on Nitrogen-Doped Carbon Nanotube Electrodes for Oxygen Reduction. *Langmuir* **2007**, *23*, 5279−5282.

(8) Mani, P.; Srivastava, R.; Strasser, P. Dealloyed Pt-Cu Core-Shell Nanoparticle Electrocatalysts for Use in PEM Fuel Cell Cathodes. *J. Phys. Chem. C* **2008**, *112*, 2770−2778.

(9) Liu, Z.; Ling, X. Y.; Su, X.; Lee, J. Y. Carbon-Supported Pt and PtRu Nanoparticles as Catalysts for a Direct Methanol Fuel Cell. *J. Phys. Chem. B* **2004**, *108*, 8234−8240.

(10) Tang, W.; Henkelman, G. Charge Redistribution in Core-Shell Nanoparticles to Promote Oxygen Reduction. *J. Chem. Phys.* **2009**, *130*, 194504.

(11) Pozun, Z. D.; Henkelman, G. A Model to Optimize the Selectivity of Gas Separation in Membranes. *J. Membr. Sci.* **2010**, *364*, 9−16.

(12) Pozun, Z. D.; Tran, K.; Shi, A.; Smith, R. H.; Henkelman, G. Why Silver Nanoparticles Are Effective for Olefin/Paraffin Separations. *J. Phys. Chem. C* **2011**, *115*, 1811−1818.

(13) Honkala, K.; Hellman, A.; Remediakis, I. N.; Logadottir, A.; Carlsson, A.; Dahl, S.; Christensen, C. H.; Nørskov, J. K. Ammonia Synthesis from First-Principles Calculations. *Science* **2005**, *307*, 555−558.

(14) Roudgar, A.; Gross, A. Local Reactivity of Metal Overlayers: Density Functional Theory Calculations of Pd on Au. *Phys. Rev. B* **2003**, *67*, 033409.

(15) Besenbacher, F.; Chorkendorff, I.; Clausen, B. S.; Hammer, B.; Molenbroek, A. M.; Nørskov, J. K.; Stensgaard, I. Design of a Surface Alloy Catalyst for Steam Reforming. *Science* **1998**, *279*, 1913−1915.

(16) Chen, J. G.; Menning, C. A.; Zellner, M. B. Monolayer Bimetallic Surfaces: Experimental and Theoretical Studies of Trends in Electronic and Chemical Properties. *Surf. Sci. Rep.* **2008**, *63*, 201−254.

(17) Newns, D. M. Self-Consistent Model of Hydrogen Chemisorption. *Phys. Rev.* **1969**, *178*, 1123−1135.

(18) Hammer, B.; Nørskov, J. K. Why Gold Is the Noblest of All the Metals. *Nature* **1995**, *376*, 238−240.

(19) Hammer, B.; Morikawa, Y.; Nørskov, J. K. CO Chemisorption at Metal Surfaces and Overlayers. *Phys. Rev. Lett.* **1996**, *76*, 2141−2144.

(20) Humbert, M. P.; Murillo, L. E.; Chen, J. G. Rational Design of Platinum-Based Bimetallic Catalysts with Enhanced Hydrogenation Activity. *ChemPhysChem* **2008**, *9*, 1262−1264.

(21) Lu, P.; Teranishi, T.; Asakura, K.; Miyake, M.; Toshima, N. Polymer-Protected Ni/Pd Bimetallic Nano-Clusters: Preparation, Characterization and Catalysis for Hydrogenation of Nitrobenzene. *J. Phys. Chem. B* **1999**, *103*, 9673−9682.

(22) Brønsted, J. N. Acid and Basic Catalysts. *Chem. Rev.* **1928**, *5*, 231−338.

(23) Evans, M. G.; Polanyi, M. Inertia and Driving Force of Chemical Reactions. *Trans. Faraday Soc.* **1938**, *34*, 11−24.

(24) Bligaard, T.; Nørskov, J. K.; Dahl, S.; Matthiesen, J.; Christensen, C. H.; Sehested, J. The Brønsted-Evans-Polanyi Relation and the Volcano Curve in Heterogeneous Catalysis. *J. Catal.* **2004**, *224*, 206−217.

(25) Logadottir, A.; Rod, T. H.; Nørskov, J. K.; Hammer, B.; Dahl, S.; Jacobsen, C. J. H. The Brønsted-Evans-Polanyi Relation and the Volcano Plot for Ammonia Synthesis over Transition Metal Catalysts. *J. Catal.* **2001**, *197*, 229−231.

(26) Vincent, T.; Guibal, E. Chitosan-Supported Palladium Catalyst. 3. Influence of Experimental Parameters on Nitrophenol Degradation. *Langmuir* **2003**, *19*, 8475−8483.

(27) Hayakawa, K.; Yoshimura, T.; Esumi, K. Preparation of Gold-Dendrimer Nanocomposites by Laser Irradiation and Their Catalytic Reduction of 4-Nitrophenol. *Langmuir* **2003**, *19*, 55−175521.

(28) Kuroda, K.; Ishida, T.; Haruta, M. Reduction of 4-Nitrophenol to 4-Aminophenol Over Au Nanoparticles Deposited on PMMA. *J. Mol. Catal. A: Chem.* **2009**, *298*, 7−11.

(29) Pradhan, N.; Pal, A.; Pal, T. Catalytic Reduction of Aromatic Nitro Compounds by Coinage Metal Nanoparticles. *Langmuir* **2001**, *17*, 1800−1802.

(30) Ghosh, S. K.; Mandal, M.; Kundu, S.; Nath, S.; Pal, T. Bimetallic Pt-Ni Nanoparticles can Catalyze Reduction of Aromatic Nitro Compounds by Sodium Borohydride in Aqueous Solution. *Appl. Catal., A* **2004**, *268*, 61−66.

(31) Scott, R. W. J.; Wilson, O. M.; Oh, S.-K.; Kenik, E. A.; Crooks, R. M. Bimetallic Palladium-Gold Dendrimer-Encapsulated Catalysts. *J. Am. Chem. Soc.* **2004**, *126*, 15583−15591.

(32) Wilson, O. M.; Scott, R. W. J.; Garcia-Martinez, J. C.; Crooks, R. M. Synthesis, Characterization, and Structure-Selective Extraction of 1−3 nm Diameter AuAg Dendrimer-Encapsulated Bimetallic Nanoparticles. *J. Am. Chem. Soc.* **2005**, *127*, 1015−1024.

(33) Panigrahi, S.; Basu, S.; Praharaj, S.; Pande, S.; Jana, S.; Pal, A.; Ghosh, S. K.; Pal, T. Synthesis and Size-Selective Catalysis by Supported Gold Nanoparticles: Study on Heterogeneous and Homogeneous Catalytic Process. *J. Phys. Chem. C* **2007**, *111*, 4596−4605.

(34) Lee, J.; Park, J. C.; Song, H. A Nanoreactor Framework of a Au@SiO$_2$ Yolk/Shell Structure for Catalytic Reduction of p-Nitrophenol. *Adv. Mater.* **2008**, *20*, 1523−1528.

(35) Wunder, S.; Lu, Y.; Albrecht, M.; Ballauff, M. Catalytic Activity of Facetted Gold Nanoparticles Studied by a Model Reaction: Evidence for Substrate-Induced Surface Restructuring. *ACS Catal.* **2011**, *1*, 908−916.

(36) Yeung, L. K.; Crooks, R. M. Heck Heterocoupling within a Dendritic Nanoreactor. *Nano Lett.* **2001**, *1*, 14−17.

(37) Hoover, N. N.; Auten, B. J.; Chandler, B. D. Tuning Supported Catalyst Reactivity with Dendrimer-Templated Pt-Cu Nanoparticles. *J. Phys. Chem. B* **2006**, *110*, 8606−8612.

(38) Ye, H.; Crooks, R. M. Effect of Elemental Composition of PtPd Bimetallic Nanoparticles Containing an Average of 180 Atoms on the Kinetics of the Electrochemical Oxygen Reduction Reaction. *J. Am. Chem. Soc.* **2007**, *129*, 3627−3633.

(39) Scott, R. W. J.; Sivadinarayana, C.; Wilson, O. M.; Yan, Z.; Goodman, D. W.; Crooks, R. M. Titania-Supported PdAu Bimetallic Catalysts Prepared from Dendrimer-Encapsulated Nanoparticle Precursors. *J. Am. Chem. Soc.* **2005**, *127*, 1380−1381.

(40) Kresse, G.; Hafner, J. Ab initio Molecular Dynamics for Liquid Metals. *Phys. Rev. B* **1993**, *47*, 558−561.

(41) Kresse, G.; Hafner, J. Ab Initio Molecular-Dynamics Simulation of the Liquid-Metal-Amorphous-Semiconductor Transition in Germanium. *Phys. Rev. B* **1994**, *49*, 14251−14269.

(42) Kresse, G.; Furthmuller, J. Efficiency of Ab-Initio Total Energy Calculations for Metals and Semiconductors Using a Plane-Wave Basis Set. *Comput. Mater. Sci.* **1996**, *6*, 15−50.

(43) Kresse, G.; Furthmüller, J. Efficient Iterative Schemes for Ab Initio Total-Energy Calculations Using a Plane-Wave Basis Set. *Phys. Rev. B* **1996**, *54*, 11169−11186.

(44) Kohn, W.; Sham, L. J. Self-Consistent Equations Including Exchange and Correlation Effects. *Phys. Rev.* **1965**, *140*, 1133−1138.

(45) Blöchl, P. E. Projector Augmented-Wave Method. *Phys. Rev. B* **1994**, *50*, 17953−17979.

(46) Kresse, G.; Joubert, D. From Ultrasoft Pseudopotentials to the Projector Augmented-Wave Method. *Phys. Rev. B* **1999**, *59*, 1758−1775.

(47) Perdew, J. P.; Wang, Y. Accurate and Simple Analytic Representation of the Electron-Gas Correlation Energy. *Phys. Rev. B* **1992**, *45*, 13244−13249.

(48) Perdew, J. P.; Chevary, J. A.; Vosko, S. H.; Jackson, K. A.; Pederson, M. R.; Singh, D. J.; Fiolhais, C. Atoms, Molecules, Solids, and Surfaces: Applications of the Generalized Gradient Approximation for Exchange and Correlation. *Phys. Rev. B* **1992**, *46*, 6671−6687.

(49) Perdew, J. P.; Chevary, J. A.; Vosko, S. H.; Jackson, K. A.; Pederson, M. R.; Singh, D. J.; Fiolhais, C. Erratum: Atoms, Molecules, Solids, and Surfaces: Applications of the Generalized Gradient Approximation for Exchange and Correlation. *Phys. Rev. B* **1993**, *48*, 4978.

(50) Vosko, S. H.; Wilk, L.; Nusair, M. Accurate Spin-Dependent Electron Liquid Correlation Energies for Local Spin Density Calculations: A Critical Analysis. *Can. J. Phys.* **1980**, *58*, 1200−1211.

(51) Methfessel, M.; Paxton, A. T. High-Precision Sampling for Brillouin-Zone Integration in Metals. *Phys. Rev. B* **1989**, *40*, 3616−3621.

(52) Welborn, M.; Tang, W.; Ryu, J.; Petkov, V.; Henkelman, G. A Combined Density Functional and X-Ray Diffraction Study of Pt Nanoparticle Structure. *J. Chem. Phys.* **2011**, *135*, 014503.

(53) Wang, Y.; Curtarolo, S.; Jiang, C.; Arroyave, R.; Wang, T.; Ceder, G.; Chen, L.-Q.; Liu, Z.-K. Ab Initio Lattice Stability in Comparison with CALPHAD Lattice Stability. *CALPHAD* **2004**, *28*, 79−90.

(54) Monkhorst, H. J.; Pack, J. D. Special Points for Brillouin-Zone Integrations. *Phys. Rev. B* **1976**, *13*, 5188−5192.

(55) Hammer, B.; Nørskov, J. K. Electronic Factors Determining the Reactivity of Metal Surfaces. *Surf. Sci.* **1995**, *343*, 211−220.

(56) Hammer, B.; Nørskov, J. K. Erratum to "Electronic Factors Determining the Reactivity of Metal Surfaces" [*Surf. Sci.* **1995**, *343*, 211]. *Surf. Sci.* **1996**, *359*, 306.

(57) Hammer, B. Special Sites at Noble and Late Transition Metal Catalysts. *Top. Catal.* **2006**, *37*, 3−16.

(58) Tang, W.; Zhang, L.; Henkelman, G. Catalytic Activity of Pd/Cu Random Alloy Nanoparticles for Oxygen Reduction. *J. Phys. Chem. Lett.* **2011**, *2*, 1328−1311.

7604

dx.doi.org/10.1021/jp312588u | *J. Phys. Chem. C* 2013, 117, 7598−7604